Inorganic Chemistry

Article

pubs.acs.org/IC

# Anionic Ordering and Thermal Properties of $FeF_3·3H_2O$

Mario Burbano,[†,‡,§] Mathieu Duttine,[‡] Olaf Borkiewicz,[∥] Alain Wattiaux,[‡] Alain Demourgues,[‡] Mathieu Salanne,[†] Henri Groult,[†] and Damien Dambournet*[,†]

[†]Sorbonne Universités, UPMC Univ Paris 06, CNRS, Laboratoire PHENIX, Case 51, 4 place Jussieu, F-75005 Paris, France

[‡]CNRS, Univ Bordeaux, ICMCB, UPR 9048, F-33600 Pessac, France

[§]Réseau sur le Stockage Electrochimique de l'Energie (RS2E), FR CNRS 3459, 80039 Amiens Cedex, France

[∥]X-ray Science Division, Advanced Photon Source, Argonne National Laboratory, 9700 South Cass Avenue, Argonne, Illinois 60439, United States

S *Supporting Information*

**ABSTRACT:** Iron fluoride trihydrate can be used to prepare iron hydroxyfluoride with the hexagonal−tungsten−bronze (HTB) type structure, a potential cathode material for batteries. To understand this phase transformation, a structural description of $\beta$-$FeF_3·3H_2O$ is first performed by means of DFT calculations and Mössbauer spectroscopy. The structure of this compound consists of infinite chains of $[FeF_6]_n$ and $[FeF_2(H_2O)_4]_n$. The decomposition of $FeF_3·3H_2O$ induces a collapse and condensation of these chains, which lead to the stabilization, under specific conditions, of a hydroxyfluoride network $FeF_{3-x}(OH)_x$ with the HTB structure. The release of $H_2O$ and HF was monitored by thermal analysis and physical characterizations during the decomposition of $FeF_3·3H_2O$. An average distribution of $FeF_4(OH)_2$ distorted octahedra in HTB-$FeF_{3-x}(OH)_x$ was obtained subsequent to the thermal hydrolysis/olation of equatorial anionic positions involving $F^-$ and $H_2O$. This study provides a clear understanding of the structure and thermal properties of $FeF_3·3H_2O$, a material that can potentially bridge the recycling of pickling sludge from the steel industry by preparing battery electrodes.

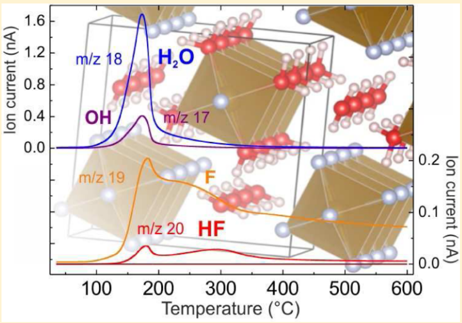

## 1. INTRODUCTION

Among the potential new positive electrode materials for batteries ($Na^+$, $Li^+$), iron fluoride combines very appealing redox properties such as a high theoretical capacity (237 mAh/g per lithium), a relatively high voltage (around 3.1−3.3 V), and a good thermal stability.[1] However, if this material is to be deployed in practical applications, its synthesis must meet rigorous cost and environmental criteria.[2] In these respects, recent work has shown that it is possible to recycle the acid and metal byproducts from the steel industry by precipitating $FeF_3·3H_2O$ from pickling liquor.[3,4] Subsequent studies by Sanghvi et al.[5] proposed and demonstrated the use of $FeF_3·3H_2O$ as a precursor for battery cathodes. In their work, $FeF_3·3H_2O$ was allowed to crystallize at room temperature from the spent liquor for a week, and upon thermal treatment it yielded the rhombohedral form of iron fluoride ($\alpha$-$FeF_3$), which when used as an electrode showed superior cycling ability compared to a commercial product. As indicated by the authors, the yield of 27% based on Fe from the hydrate precipitation remains to be improved, which could likely be achieved by thermal activation. Further enhancements of the electrochemical properties of the end product are also likely to result from an optimized decomposition of $\beta$-$FeF_3·3H_2O$. It is thus necessary to glean a better understanding of the thermal properties of $FeF_3·3H_2O$ if it is to be a viable precursor for battery cathodes.

Several procedures have been developed to prepare iron fluoride from the thermal decomposition of $\beta$-$FeF_3·3H_2O$ (henceforth $FeF_3·3H_2O$). Depending on the protocol, different compounds have been obtained ranging from amorphous to various forms of crystallized compounds, thus emphasizing a complex thermal decomposition path.[6−8] Li et al.[9] showed that the thermal decomposition of $FeF_3·3H_2O$ in an ionic liquid can yield $FeF_3·0.33H_2O$ with the hexagonal−tungsten−bronze (HTB)[10] type and attempted to provide a structural relationship between these two compounds. Nevertheless, the structure of $FeF_3.3H_2O$ depicted by the authors is unreasonable with heavily distorted $FeF_4(H_2O)_2$ octahedra probably due to an uncorrected choice of crystallographic origin during crystal structure drawing.

In the present Article, we investigate the crystal structure of $FeF_3·3H_2O$ by means of Rietveld analysis of X-ray diffraction data, DFT calculations, and Mössbauer spectroscopy. The results point toward a structure featuring ordered $FeF_6$ and $FeF_2(H_2O)_4$ octahedra as opposed to the average $FeF_4(H_2O)_2$ crystal unit. A comprehensive study of the thermal behavior of $FeF_3·3H_2O$ was also undertaken using thermogravimetric analysis combined with mass spectrometry.

**Received:** July 28, 2015
**Published:** September 17, 2015

DOI: 10.1021/acs.inorgchem.5b01705

## 2. EXPERIMENTAL AND COMPUTATIONAL METHODS

**2.1. Synthesis of $FeF_3·3H_2O$.** $FeF_3·3H_2O$ was precipitated from an aqueous solution containing $Fe^{3+}$ nitrate nonahydrate ($Fe(NO_3)_3·9H_2O$) and hydrofluoric acid (HF, Rectapur, 40%). A 0.042 mol portion of $Fe^{3+}$ salt was dissolved in 42 mL of distilled water. A 0.168 mol portion of HF, corresponding to a F/Fe molar ratio equal to 4, was added to the solution. The precipitation was thermally assisted by microwave heating performed in a microwave-accelerated reaction system MARS5 (CEM corporation) operating at 2.45 GHz with a power supply of 900 W. As previously reported,[11] the microwave-assisted synthesis consists of two successive steps including activation and drying processes. For the former, the solution was heated up to the synthesis temperature (90 °C) within 5 min, and further kept for 30 min. Thereafter, the solution was cooled down to room temperature. The drying step was performed at 90 °C under nitrogen gas stream and primary vacuum (~500 mbar). The obtained powder was washed by ultrafiltration using ethanol and nitrogen gas flow. Finally, the powder was outgassed at 90 °C under vacuum for 2 h.

**2.2. Decomposition under Self-Generated Atmosphere.** In a typical procedure, 0.5 g of $FeF_3·3H_2O$ was placed in an alumina crucible. To obtain a self-generated atmosphere produced during the decomposition process of $FeF_3·3H_2O$, the crucible was rolled tightly in aluminum foil. The sample was then placed in a tubular oven which was progressively heated at 5 °C/min under air and left at the desired temperature for 2 h. Thereafter, the oven was cooled down to RT, and the sample was recovered.

**2.3. Thermal Analyses.** Thermogravimetric analysis (TGA) was performed using Setaram Setsys evolution that was coupled with a mass spectrometer (MS) (Pfeiffer Ominstar) allowing the detection of HF and water departures. Samples were heated from room temperature up to 600 °C under helium atmosphere (heating rate 5 °C/min).

**2.4. X-ray Diffraction (XRD) Analysis.** Powder XRD patterns were recorded on PANalytical X'Pert (Co K$\alpha$ or Cu K$\alpha_1$ radiation) diffractometers in a Bragg–Brentano geometry ($\theta$–2$\theta$). Structural analysis was performed using Le Bail and Rietveld methods as implemented in the FULLPROF software.[12]

**2.5. Mössbauer Spectroscopy.** Measurements were performed at room temperature using a constant acceleration Halder type spectrometer with a room temperature $^{57}Co$ source in transmission geometry. The velocity was calibrated using pure $\alpha$-Fe as the standard material. Mossbauer spectra were reconstructed using the WinNormos software.[13]

**2.6. Pair Distribution Function (PDF) Analysis.** Samples were packed in Kapton capillaries. High-energy X-ray data were collected at the 11-ID-B station at the Advanced Photon Source (Argonne National Laboratory). After corrections (background and Compton scattering), PDFs were extracted from the data using PDFgetX2 sofware.[14] Refinements of the PDF data were performed using PDFgui.[15]

**2.7. Computational Methods.** The structure and total energy of the bulk compounds $FeF_3·3H_2O$ and $FeF_3$-HTB, as well as the defects in the $FeF_3$-HTB cells, were studied using the plane-wave DFT implementation found in the VASP code.[16,17] The Perdew–Burke–Ernzerhof (PBE) GGA exchange-correlation functional was supplemented by the Dudarev + *U* correction in order to describe correctly the strongly correlated Fe 3d states. A value of *U*Fe(d) = 5.3 eV was used as is the case for the iron oxyfluorides studied in the Materials Genome project.[18] Valence–core interactions were represented by means of the projector-augmented wave (PAW) approach.[19,20] In the case of the 12 $FeF_3·3H_2O$ configurations investigated, structural optimizations were performed with the VASP tag ISIF = 3, that allows the shape, volume, and ionic positions to be relaxed. The optimal $FeF_3$-HTB structure was obtained by performing multiple relaxations at constant volume in order to fit to the Murnaghan[21] equation of state. This method avoids the problems of Pulay stress and changes in basis set which are intrinsic to plane wave calculations. A plane wave cutoff of 500 eV was used throughout all the calculations, with well-converged *k*-point sampling for each system, i.e., 4 × 4 × 6 for $\beta$-$FeF_3·3H_2O$ and 4 × 2 × 4 for $FeF_3$-HTB, both Γ-centered. All calculations were spin polarized and were initialized assuming a high-spin ferromagnetic ordering for the Fe ions.[22] Structural optimizations were considered converged when the force on every ion was less than 0.01 eV/ Å.

## 3. RESULTS AND DISCUSSION

**3.1. Structural Analysis of $FeF_3·3H_2O$.** Iron fluoride trihydrate was synthesized using a precipitation method performed in aqueous medium by a microwave-assisted hydrothermal process. The yield of the reaction was ca. 85% based on Fe. This method could be easily applied to prepare iron fluoride from steel pickling liquor. The prepared solid exhibited large micrometric particles with irregular shape (Figure S1 in Supporting Information). The phase purity was confirmed by indexation of the X-ray diffraction pattern using a tetragonal symmetry corresponding to iron fluoride trihydrate $FeF_3·3H_2O$. The crystal structure of $FeF_3·3H_2O$ was studied by Rietveld analysis of the XRD pattern (Figure 1). Full pattern profile refinement of the XRD pattern yielded the following unit cell parameters $a = b = 7.8327(2)$ Å and $c = 3.8754(1)$ Å, in good agreement with literature data.[23]

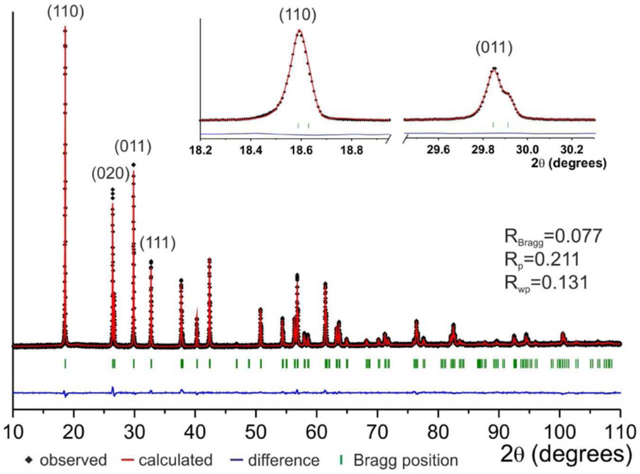

**Figure 1.** Rietveld refinement of the X-ray diffraction pattern (Co K$\alpha$ source) of $FeF_3·3H_2O$.

Rietveld analysis was performed using a structural model based on the aluminum analogue $AlF_3·3H_2O$[24,25] (space group: *P*4/*n*). The final reliability structural factor was satisfactory with $R_{Bragg} = 7.7\%$. Structural parameters are gathered in Supporting Information (Table S1).

The refinement confirms that $FeF_3·3H_2O$ is isostructural to the Al-homologue, whose structure is built from infinite chains of corner-sharing $FeF_4(H_2O)_2$, slightly distorted octahedra held by structural hydrogen-bonds from water (Figure 2a). The axial F atoms displayed a Fe–F distance of 1.920(4) and 1.955(4) Å while the equatorial positions show distances of 1.9947(13) Å. The equatorial positions of the octahedra (8g Wyckoff site) are predicted by the crystal symmetry to be statistically occupied by two fluoride and two water molecules, yielding $FeF_4(H_2O)_2$ octahedra as the average building block. However, this average picture does not enable a full description of the local $Fe^{3+}$ environment as anion ordering can occur at this site.

In order to establish the possible speciation of $Fe^{3+}$, we carried out atomistic simulations of all the possible configurations as given by the symmetry of the cell. These were

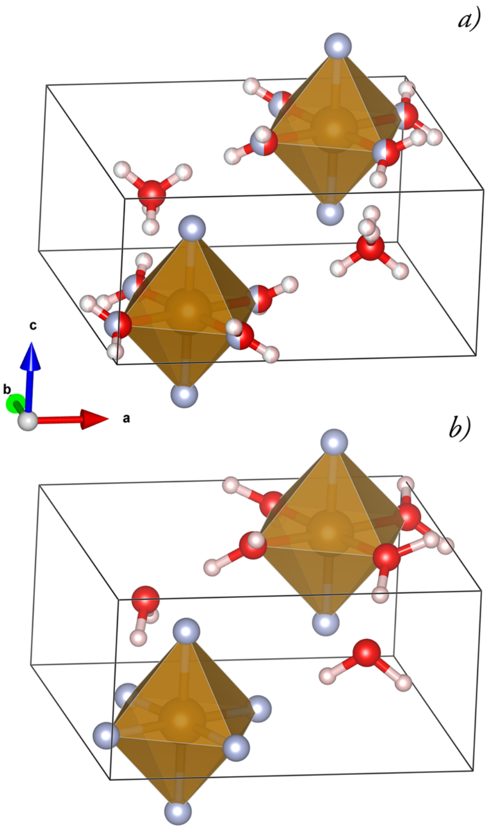

**Figure 2.** (a) Structure of $FeF_3 \cdot 3H_2O$ with partial occupancies in the equatorial positions of the octahedra (8g Wyckoff site). (b) Lowest energy configuration obtained by atomic simulation highlighting an anionic ordering.

generated by the site occupancy disorder (SOD) program by Grau-Crespo et al.[26] In this case, SOD used the symmetry operations of the space group $P4/n$ of the cell to generate 12 unique configurations that account for the partially occupied equatorial positions by fluoride and water molecules. These 12 configurations correspond to the occurrence of different anionic environments in $Fe^{3+}$ octahedra such as $FeF_{6-x}(H_2O)_x$, with $0 \leq x \leq 4$. Each of these configurations was subsequently relaxed using density functional theory (DFT) in order to find the most stable (see Computational Methods for more details). The resulting energies along with the probabilities of formation at 300 K for the 12 configurations (Table S2) unambiguously pointed toward a unique stable configuration, namely configuration 1 (Figure 2b). The predicted structure parameters and bond lengths of this configuration are given in Table S3. From Figure 2b it is clear that there exists anionic ordering in this structure because in this case various anions, $F^-$, and $H_2O$ are segregated into the equatorial positions, revealing the existence of two types of $Fe^{3+}$ octahedra in equal proportions, $FeF_6$ and $FeF_2(H_2O)_4$, which are stacked along the $c$-axis in chains.

To get further confirmation of the existence of the extended $FeF_6$ and $FeF_2(H_2O)_4$ chains along the $c$-axis, we generated a 1 × 1 × 2 supercell for configuration 1 and a second cell of the same dimensions, but with an alternating stacking of the Fe octahedra along the $c$-axis as shown in Figure 3a,b, respectively. These two different configurations were subsequently relaxed using DFT in order to obtain their energies; the results (per formula unit) indicate that the system with chains of either $FeF_6$ or $FeF_2(H_2O)_4$ octahedra along the $c$-axis has a lower energy (−65.689 54 eV) compared to that in which the $FeF_6$ or $FeF_2(H_2O)_4$ octahedra alternate along this direction (−65.092 79 eV). This energy difference and the large

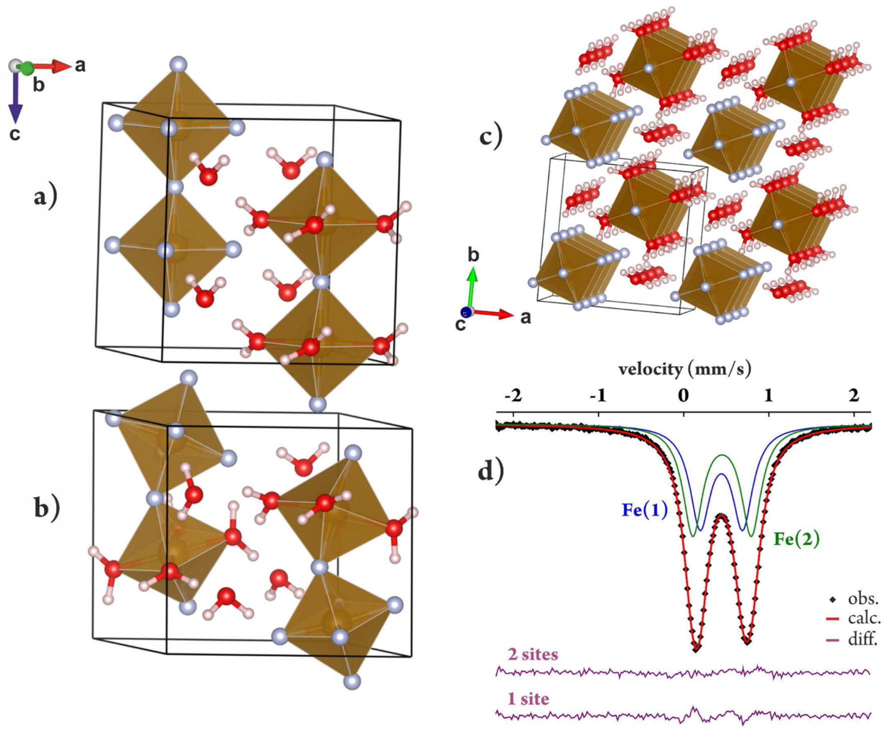

**Figure 3.** (a) 1 × 1 × 2 supercell of the lowest energy configuration (configuration 1). (b) Supercell with alternating $FeF_6$ and $FeF_2(H_2O)_4$ octahedra along the $c$-axis. (c) Extended cell of the lowest energy configuration. (d) Mössbauer spectrum of $\beta$-$FeF_3 \cdot 3H_2O$ reconstructed using two $Fe^{3+}$ signals, Fe(1) (blue) and Fe(2) (green). The difference between the observed and calculated values is represented as violet lines.

distortions undergone in the system with alternating octahedra indicate that $FeF_3·3H_2O$ is likely to adopt a configuration like that shown in Figure 3c.

The local environment of $Fe^{3+}$ in $FeF_3·3H_2O$ was also probed experimentally using Mössbauer spectroscopy. In order to compare the different structural models predicted either by the crystal symmetry or by DFT calculations, the Mössbauer spectrum was reconstructed using one or two different $Fe^{3+}$ environments (Figure 3d). The best fit was provided using the two different $Fe^{3+}$ environments in agreement with DFT calculations. In particular, it enables accounting for the asymmetric character of the doublet. The resulting Mössbauer parameters are presented in Table 1. The two signals display similar isomer shift values, e.g., 0.45 mm/s, characteristic of trivalent iron in a 6-fold coordination mode. The relative intensity indicated that the two signals are in equal proportion, which is in agreement with the predictions from DFT calculations. Moreover, both signals differed only by their quadrupole splitting $\Delta E_Q$ value, which reflects the distortion of the $Fe^{3+}$ octahedral related to various anionic environment. The quadrupole splitting arises mainly from the lattice contribution to the electric field gradient (EFG) through the crystal field produced by ligands at the $^{57}Fe$ nucleus. Therefore, the $FeF_6$ environment likely shows a lower quadrupole splitting than $FeF_2(H_2O)_4$. As a result, signals 1 and 2 were assigned to $FeF_6$ and $FeF_2(H_2O)_4$, respectively (Table 1).

**Table 1. $^{57}Fe$ Mössbauer Parameters of $FeF_3·3H_2O$ Obtained from the Reconstruction of Spectra Shown in Figure 3d and Their Assignments**[a]

| | signal | |
|---|---|---|
| | $Fe^{3+}$ [6] (1) | $Fe^{3+}$ [6] (2) |
| $\delta$ (mm/s) | 0.44(1) | 0.45 (1) |
| $\Delta E_Q$ (mm/s) | 0.50(1) | 0.69(1) |
| $\Gamma$ (mm/s) | 0.29(1) | 0.28(1) |
| area (%) | 49.3(5) | 50.7(5) |
| assignment | $FeF_6$ | $FeF_2(H_2O)_4$ |

[a] $\delta$ = isomer shift relative to $\alpha$-iron standard, $^{57}Co$ (Rh) source; $\Delta E_Q$ = quadrupole splitting; $\Gamma$ = lorentzian line width.

**3.2. Thermal Analysis of $FeF_3·3H_2O$.** The thermal behavior of $FeF_3·3H_2O$ was studied by means of thermogravimetric analysis (TGA) coupled with a mass spectrometer under helium atmosphere (Figure 4). The results of this analysis reveal two distinct steps in the decomposition of $FeF_3·3H_2O$ as observed in the change of slope of the TGA curve. These steps were assigned to the stabilization of HTB-structured $FeF_3·(H_2O)_{0.33}$ and to $\alpha$-$FeF_3$ at high temperature, respectively.

The analysis by mass spectrometry emphasized a complex thermal decomposition process with the detection of gaseous hydrofluorhydric acid (HF) in addition to the expected water vapor. The monitoring of the ionic curves of the mass fragments $m/z = 17$ ($OH^+$), 18 ($H_2O^+$), 19 ($F^+$), and 20 ($HF^+$) enabled a better understanding of the thermal decomposition process of $FeF_3·3H_2O$. The first thermogravimetric event occurred within the 30−240 °C range at a DTG maximum around 170 °C leading to 30% wt loss (Figure 4, bottom). During this step, the mass spectrometer detected the release of $H_2O$ and HF indicating concomitant dehydration and hydrolysis reactions. The detection of HF emphasized a partial replacement of Fe−F by Fe−OH bonds,[27] which indicates that this initial stage of the process likely involved the stabilization of a hydroxylated HTB type structure rather than a pure fluoride. During this step, the release of the structural water from $FeF_3·3H_2O$ induced the collapse of the structure followed by the concomitant condensation of the 1D chains of $[FeF_2(H_2O)_4]_n$ and $[FeF_6]_n$ with subsequent dehydration and hydrolysis as follows:

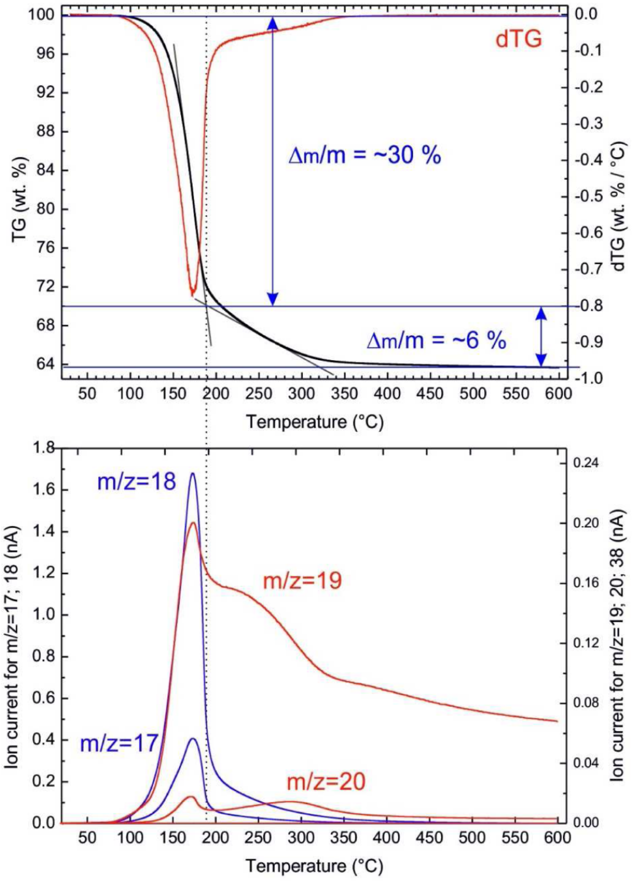

**Figure 4.** Thermogravimetric (top) and mass spectrometry (bottom) analyses of $\beta$-$FeF_3·3H_2O$ performed under He.

$$FeF_3·3H_2O \rightarrow FeF_{3-x}(OH)_x·(H_2O)_y + xHF + (3-x-y)H_2O, \quad \text{where } y \leq 0.33 \qquad (1)$$

The second step occurred within the 240−440 °C temperature range and led to 6 wt % loss. The mass spectrometry data indicated the continuous release of both water and HF. The release of $H_2O$ arises from the removal of structural water and dehydroxylation reaction of the HTB type structure. The departure of HF might result from the continuous hydrolysis of the structure during its transformation toward $\alpha$-$FeF_3$.

The rate of hydrolysis was quantified by the analysis of the XRD pattern obtained from the powder recovered after the TGA measurement, i.e., up to 600 °C. Rietveld analysis (Figure S2) led to an estimated molar percentage of 16% and 84% for $Fe_2O_3$ and $\alpha$-$FeF_3$, respectively. The overall reaction that takes place during the thermal decomposition of $FeF_3·3H_2O$ can thus be summarized as follows:

$$FeF_3·3H_2O \rightarrow 0.84\alpha\text{-}FeF_3 + 0.08Fe_2O_3 + 0.48HF + 2.76H_2O \qquad (2)$$

The theoretical weight loss associated with the above reaction was $\Delta m/m \times 100 = 35.5\%$, in good agreement with the experimental data (36.3%). This weight loss is close to that calculated for a simple dehydration process, $FeF_3{\cdot}3H_2O \rightarrow FeF_3 + 3H_2O$ (weight loss: 32.4%), which might cause misinterpretation. This is due to the fact that exchanges of F/OH only slightly affect the mass variation and thus cannot be probed properly by using thermogravimetric analysis alone.[27]

### 3.3. Optimized Decomposition Process of $FeF_3{\cdot}3H_2O$.

The thermal analysis of $FeF_3{\cdot}3H_2O$ indicated that this compound can be used as a precursor for the preparation of the HTB framework, a potential cathode material for batteries.[11] However, it also revealed that the HTB phase exhibits a narrow range of stability with respect to temperature since the decomposition process can yield $\alpha$-$FeF_3$. The range of existence of intermediate compositions/structures can be extended by means of the self-generated atmosphere method,[28] where the decomposition of the metal fluoride hydrate takes place in a closed container.

We tested this strategy by performing two $FeF_3{\cdot}3H_2O$ decompositions at 130 °C for 2 h, one under air and another under a self-generated atmosphere (see Experimental and Computational Methods section for details). X-ray diffraction analysis (Figure 5) showed that the sample that decomposed under an air atmosphere (blue) is amorphous. A combination of pair distribution function and Mossbauer spectroscopy has revealed that the sample decomposed under air and consisted of a phase mixture of the HTB and $\alpha$-$FeF_3$.[8] In contrast, the use of the self-generated atmosphere led to the stabilization of a pure and well-crystallized compound whose pattern was indexed with an orthorhombic symmetry characteristic of the HTB type structure.

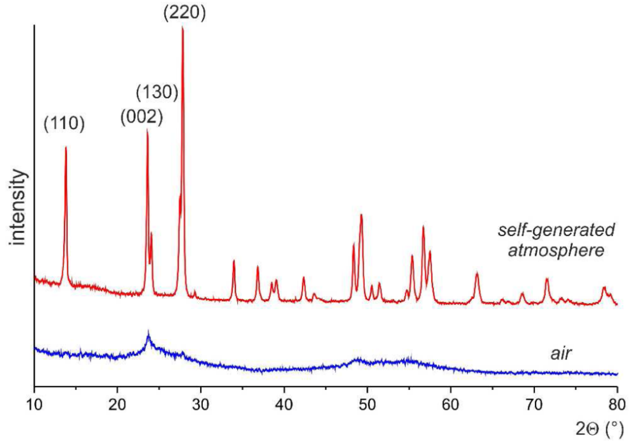

**Figure 5.** X-ray diffraction powder patterns of $FeF_3{\cdot}3H_2O$ decomposed at 130 °C under air (for 2 h) with and without the self-generated atmosphere method.

The decomposition of $FeF_3{\cdot}3H_2O$ under self-generated atmosphere was monitored by high-energy X-ray diffraction starting from low temperature, i.e., 100 °C, to 130 °C (Figure 6). Under these conditions, $FeF_3{\cdot}3H_2O$ readily decomposed into the HTB-type structure at $T > 100$ °C and is obtained as a single phase at ca. $T = 130$ °C. Extending the decomposition process within the temperature range 130−220 °C still enabled the stabilization of the HTB-type structure showing that this condition clearly allows stabilizing intermediate phases.

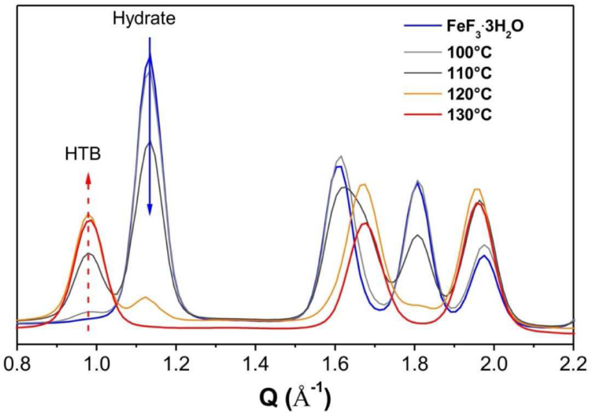

**Figure 6.** High-energy X-ray diffraction powder patterns of $FeF_3{\cdot}3H_2O$ decomposed at different temperatures under self-generated atmosphere.

### 3.4. Structural Characterization of the HTB Framework.

Similarly to our previous study on amorphous $FeF_3$, structural insight of the HTB phase was obtained by the pair distribution functions and Mössbauer spectroscopy.[8]

The refinement of the PDF using the real space method confirms that the phase is pure without any amorphous component. Thus, the refinement of the PDF using HTB-type structure provides a good fit to the data (Figure 7).

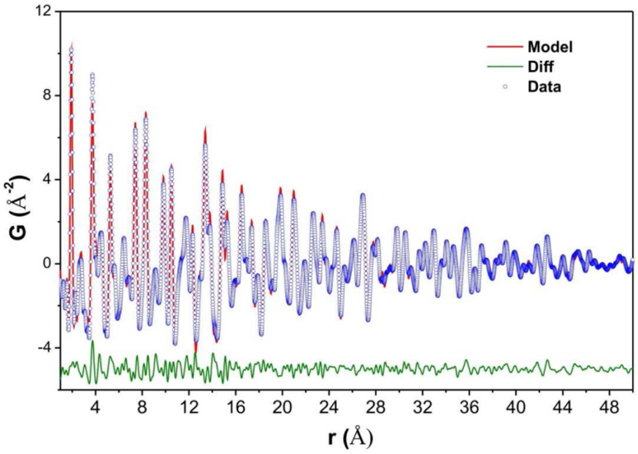

**Figure 7.** Refinement of the PDF of the phase prepared by thermal decomposition of $FeF_3{\cdot}3H_2O$ decomposed at 130 °C under self-generated atmosphere.

Crystal parameters (Table S4) reveal a broad distribution of interatomic distances that range from 1.883 to 1.986 Å and larger unit cell parameters which are due to the presence of OH groups partially substituting fluoride. Samples prepared at higher temperatures, i.e., $130 < T \leq 220$ °C, displayed similar crystal parameters characteristic of a hydroxyfluoride composition (Table S4), which suggests that the temperature only slightly impacts the rate of hydrolysis. The presence of OH groups was further confirmed by $^{57}$Fe Mössbauer spectroscopy. The spectrum obtained (Figure 8) may be analyzed using distributions of both isomer shift and quadrupole splitting, i.e., the sum of quadrupole doublets with Lorentzian shape (line width 0.26 mm/s), isomer shift ranging from 0.41 to 0.45 mm/s, and different quadrupole splitting values, due to the presence of oxygen in the vicinity of $Fe^{3+}$. Furthermore, this shows that

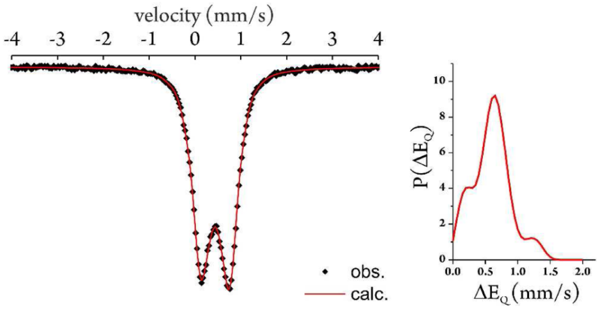

| assign. | δ (mm/s) | ΔE$_Q$ (mm/s) | Γ (mm/s) | area (%) |
|---|---|---|---|---|
| $Fe^{3+}$ | 0,43* | 0,60* | 0,26(-) | 100 |

**Figure 8.** $^{57}$Fe Mössbauer spectra of HTB-$FeF_{3-x}(OH)_x$ hydroxyfluoride. Right panel: Quadrupole splitting distributions. $^{57}$Fe Mossbauer parameters obtained from the reconstruction of spectra are shown in left. * indicates average value.

the $Fe^{3+}$ ions exhibited different types of anionic environments with different F/OH ratios and heterogeneous interatomic distances in the $FeF_{6-x}(OH)_x$ octahedra.

Thermal analysis (Figure S3) performed on the hydroxyfluoride revealed a combined departure of HF and $H_2O$ at $T >$ 130 °C, thus preventing the determination of an accurate OH content. Nevertheless, the chemical composition of the hydroxyfluoride phase obtained by decomposition of $FeF_3 \cdot 3H_2O$ is close to $FeF_{2.2}(OH)_{0.8}$.[27] This trend is also supported by the hydrolysis rate deduced by Rietveld analysis/TGA (cf. eq 2, and Figures S2 and S3). Then, in as-obtained HTB Fe hydroxyfluoride, the average octahedron is associated with the following chemical formulas $FeF_4(OH)_2$. The release of $H_2O$ and HF during the decomposition of $FeF_3 \cdot 3H_2O$ with two kind of octahedra $FeF_6$ and $FeF_2(H_2O)_4$ forming infinite chains leads to an average distribution of $FeF_4(H_2O)_2$ distorted octahedra in HTB-$FeF_{3-x}(OH)_x$ consecutive to the thermal olation of equatorial anion position involving $F^-/H_2O$.

### 3.5. Discussion on the Decomposition of $FeF_3 \cdot 3H_2O$ into HTB-$FeF_{3-x}(OH)_x$.

The structure of $FeF_3 \cdot 3H_2O$ was found to be built from infinite chains of $[FeF_6]_n$ and $[FeF_2(H_2O)_4]_n$ held by water molecules. The stabilization from the trihydrate phase toward the HTB type structure points out two features: (i) the role of the atmosphere to favor the formation of the HTB type structure and (ii) the hydrolysis occurring during the collapse of the $FeF_3 \cdot 3H_2O$ phase.

The decomposition of $FeF_3 \cdot 3H_2O$ toward the HTB structure implies the concomitant condensation of $[FeF_6]_n$ and $[FeF_2(H_2O)_4]_n$ chains yielding a hydroxyfluoride $FeF_{3-x}(OH)_x$ network. Very likely, water vapor produced by the self-generated atmosphere process favors the formation of the HTB type structure. Nevertheless, the generation of OH groups during this process might also play a role in stabilizing the HTB structure at the expense of the distorted $ReO_3$ type structure ($\alpha$-$FeF_3$). To test this hypothesis, DFT simulations were used to calculate the formation energies of $OH^-$ substitutions on the $F^-$ anion sublattice in both the HTB and the distorted $ReO_3$ type structures. These energies were calculated from the energies of the relaxed cells for the pure and substituted systems (see Computational Methods). The converged cells are presented in Figure 9. The four different anion positions in the HTB cell are labeled F1, F2, F3, and F4; the distorted $ReO_3$ structure displays one anionic site only. The DFT calculations predict bond lengths of ca. 1.960 and 1.957 Å for the Fe−F distances of the HTB (Table S5) and distorted $ReO_3$-type structures, respectively, which agree with experimental data.[29] The formation energies of single and double $OH^-$ substitutions on the $F^-$ anion sublattice in both the HTB and distorted $ReO_3$-type structure are presented in Table 2 using Kröger−Vink notation; e.g., $OH_F$ represents a OH substitution for $F^-$. The results show that $OH^-$ substitution for $F^-$ is more favorable in all the different F sites of the HTB-type structure than in $ReO_3$-structured $FeF_3$. This highlights the need for a self-generated atmosphere in the stabilization of HTB-$FeF_3$ from $FeF_3 \cdot 3H_2O$, because, as these values indicate, an uncontrolled reaction is likely to yield fluoride ($\alpha$-$FeF_3$) and oxide phases as suggested by experimental observations.[5]

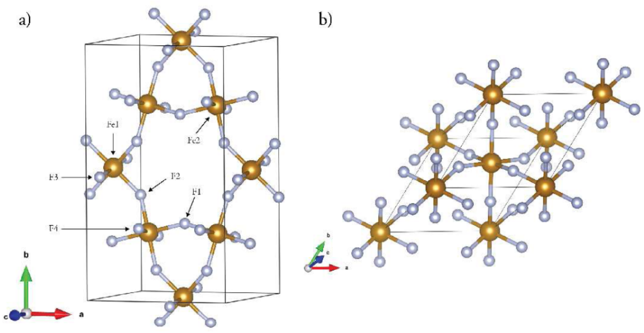

**Figure 9.** Converged structures of the (a) $FeF_3$-HTB and (b) $\alpha$-$FeF_3$ phases. Fe and F atoms are represented by brown and blue spheres, respectively. In the case of $FeF_3$-HTB, the different Fe and F positions are labeled, and only one layer of atoms along the *c*-axis is shown in order to facilitate visualization.

**Table 2. DFT Calculated Formation Energies for $OH^-$ Substitution in the $F^-$ Sublattice of HTB and Distorted $ReO_3$ Type $FeF_3$ (eV/formula unit)**

| defect | energy (eV/formula unit) |
|---|---|
| $OH_{F1}$ | 0.011 |
| $OH_{F2}$ | 0.013 |
| $OH_{F3}$ | 0.020 |
| $OH_{F4}$ | 0.021 |
| $OH_F$ ($ReO_3$) | 0.027 |

It is worth noting that, within the HTB structure, the $OH_{F1}$ and $OH_{F2}$ substitutions were found to have the lowest formation energies compared to $OH_{F3}$ and $OH_{F4}$, which indicates that the fluoride substitution by OH groups is favored within the hexagonal section of the network. A structural comparison between $FeF_3 \cdot 3H_2O$ and the HTB structure shows that the HTB F1 and F2 sites result from the condensation of the equatorial positions of $FeF_6$ and $FeF_2(H_2O)_4$ octahedra from $FeF_3 \cdot 3H_2O$. This implies that F1 and F2 sites are likely partially hydroxylated while F3 and F4 sites that derive from the axial fluoride sites in $FeF_3 \cdot 3H_2O$ are fluorinated sites.

## 4. CONCLUSIONS

The combination of experimental and computational tools employed in this study allowed a complete determination of the atomic structure of $FeF_3 \cdot 3H_2O$. Rietveld analysis of the powder X-ray diffraction pattern of this compound yielded an average description of the structure with a building unit consisting of

$FeF_4(H_2O)_2$ octahedra. However, DFT and Mössbauer spectroscopy pointed toward the existence of two distinct $Fe^{3+}$ environments with $FeF_6$ and $FeF_2(H_2O)_4$ octahedra yielding a structure built from infinite chains of $[FeF_6]_n$ and $[Fe_2(H_2O)_4]_n$ held by hydrogen bonds.

Thermal analysis revealed that the decomposition of $FeF_3 \cdot 3H_2O$ involves the intercondensation of these chains of $[FeF_6]_n$ and $[Fe_2(H_2O)_4]_n$ through hydrolysis and dehydration/olation reactions. Thus, the decomposition of chains of $FeF_3 \cdot 3H_2O$ produces a mixed anionic compound whose structure is dictated by the decomposition conditions. The use of a self-generated atmosphere favors the stabilization of the hexagonal−tungsten−bronze type structure with OH groups being partially substituted for fluoride anions due to hydrolysis. This phase can be used as an electrode for batteries.

## ■ ASSOCIATED CONTENT

### Ⓢ Supporting Information

The Supporting Information is available free of charge on the ACS Publications website at DOI: 10.1021/acs.inorgchem.5b01705.

Complementary data including structural data, TGA, SEM, and DFT calculations (PDF)

## ■ AUTHOR INFORMATION

### Corresponding Author

*E-mail: damien.dambournet@upmc.fr.

### Notes

The authors declare no competing financial interest.

## ■ ACKNOWLEDGMENTS

The research leading to these results has received funding from the People Programme (Marie Curie Actions) of the European Union's Seventh Framework Programme (FP7/2007-2013) under REA grant agreement no. [321879] (FLUOSYNES). We also thank the Hydro-Québec Company and the University Pierre and Marie Curie for funding. The work done at the Advanced Photon Source, an Office of Science User Facility operated for the U.S. Department of Energy (DOE) Office of Science by Argonne National Laboratory, was supported by the U.S. DOE under Contract DE-AC02-06CH11357.

## ■ REFERENCES

(1) Pereira, N.; Badway, F.; Wartelsky, M.; Gunn, S.; Amatucci, G. G. *J. Electrochem. Soc.* **2009**, *156*, A407−A416.

(2) Larcher, D.; Tarascon, J.-M. *Nat. Chem.* **2015**, *7*, 19−29.

(3) Forsberg, K. M.; Rasmuson, Å. C. *J. Cryst. Growth* **2006**, *296*, 213−220.

(4) Forsberg, K. M.; Rasmuson, Å. C. *Miner. Eng.* **2007**, *20*, 950−955.

(5) Sanghvi, S.; Pereira, N.; Halajko, A.; Amatucci, G. G. *RSC Adv.* **2014**, *4*, 57098−57110.

(6) Kim, S.-W.; Seo, D.-H.; Gwon, H.; Kim, J.; Kang, K. *Adv. Mater.* **2010**, *22*, 5260−5264.

(7) Liu, L.; Guo, H.; Zhou, M.; Wei, Q.; Yang, Z.; Shu, H.; Yang, X.; Tan, J.; Yan, Z.; Wang, X. *J. Power Sources* **2013**, *238*, 501−515.

(8) Dambournet, D.; Duttine, M.; Chapman, K. W.; Wattiaux, A.; Borkiewicz, O.; Chupas, P. J.; Demourgues, A.; Groult, H. *J. Phys. Chem. C* **2014**, *118*, 14039−14043.

(9) Li, C.; Yin, C.; Mu, X.; Maier, J. *Chem. Mater.* **2013**, *25*, 962−969.

(10) Leblanc, M.; Ferey, G.; Chevallier, P.; Calage, Y.; De Pape, R. *J. Solid State Chem.* **1983**, *47*, 53−58.

(11) Duttine, M.; Dambournet, D.; Penin, N.; Carlier, D.; Bourgeois, L.; Wattiaux, A.; Chapman, K. W.; Chupas, P. J.; Groult, H.; Durand, E.; Demourgues, A. *Chem. Mater.* **2014**, *26*, 4190−4199.

(12) Rodríguez-Carvajal, J. *Commission on POWDER Diffraction Newsletter* **2001**, *26*, 12.

(13) Brand, R. *WinNormos Software*; Universität Duisburg-Essen: Duisburg, Germany, 2008.

(14) Qiu, X.; Thompson, J. W.; Billinge, S. J. L. *J. Appl. Crystallogr.* **2004**, *37*, 678−678.

(15) Farrow, C. L.; Juhas, P.; Liu, J. W.; Bryndin, D.; Božin, E. S.; Bloch, J.; Proffen, T.; Billinge, S. J. L. *J. Phys.: Condens. Matter* **2007**, *19*, 335219.

(16) Kresse, G.; Hafner, J. *Phys. Rev. B: Condens. Matter Mater. Phys.* **1994**, *49*, 14251−14269.

(17) Kresse, G.; Furthmüller, J. *Phys. Rev. B: Condens. Matter Mater. Phys.* **1996**, *54*, 11169−11186.

(18) Jain, A.; Ong, S. P.; Hautier, G.; Chen, W.; Richards, W. D.; Dacek, S.; Cholia, S.; Gunter, D.; Skinner, D.; Ceder, G.; Persson, K. a. *APL Mater.* **2013**, *1*, 011002.

(19) Blöchl, P. E. *Phys. Rev. B: Condens. Matter Mater. Phys.* **1994**, *50*, 17953−17979.

(20) Kresse, G.; Joubert, D. *Phys. Rev. B: Condens. Matter Mater. Phys.* **1999**, *59*, 1758−1775.

(21) Murnaghan, F. D. *Proc. Natl. Acad. Sci. U. S. A.* **1944**, *30*, 244−247.

(22) Chevrier, V. L.; Hautier, G.; Ong, S. P.; Doe, R. E.; Ceder, G. *Phys. Rev. B: Condens. Matter Mater. Phys.* **2013**, *87*, 094118.

(23) Teufer, G. *Acta Crystallogr.* **1964**, *17*, 1480.

(24) Chupas, P. J.; Corbin, D. R.; Rao, V. N. M.; Hanson, J. C.; Grey, C. P. *J. Phys. Chem. B* **2003**, *107*, 8327−8336.

(25) Kemnitz, E.; Groß, U.; Rüdiger, S.; Scholz, G.; Heidemann, D.; Troyanov, S. I.; Morosov, I. V.; Lemée-Cailleau, M.-H. *Solid State Sci.* **2006**, *8*, 1443−1452.

(26) Grau-Crespo, R.; Hamad, S.; Catlow, C. R. A.; Leeuw, N. H. de. *J. Phys.: Condens. Matter* **2007**, *19*, 256201.

(27) Feist, M.; Kemnitz, E. *Thermochim. Acta* **2006**, *446*, 84−90.

(28) Menz, D. H. *J. Therm. Anal.* **1992**, *38*, 321−334.

(29) Leblanc, M.; Pannetier, J.; Férey, G.; Pape, R. D. *Rev. Chim. Miner.* **1985**, *22*, 107−114.